Proceedings of the 2024 IEEE
International Conference on Cyborg and Bionic Systems
Nagoya, Japan, November 20-22, 2024

Motion Analysis and Design of Bionic Swimming Robot

Yuanshao Yang[1,*], Mingkai Xia[1,*], Naike Wu[1,*], and Junhan Zhang[1,*]

***Abstract*— Targeting transport is an emerging field in the medical industry that is attempting to obtain a more precise cure for the diseased area. This transport process requires a robot transporter to reach the target.**

This project aims to develop an E. coli-based swimming robot for precisely delivering medicine to the appointed target area.

Key parameters influencing motion are selected through preliminary kinematic analysis in a uniform, viscous fluid. By using the recursion method and differential equation calculation, this project simulated the trajectory related to the robot's movement and derived the controlling equation. Computer Aided Design (CAD) models are developed under macroscopic dimensions and simulations are performed in liquid environments for validation under microscopic dimensions. A path planning algorithm and a control program with feedback and feedforward control are also developed to stabilize the system.

This project has tested the feasibility of different motions under different sets of design specifications and thrust setups, and optimized the related design specifications in the unified viscous flow by Computational Fluid Dynamics (CFD) analysis. In addition, a control system for the swimmer's obstacle avoidance and path planning was designed, based on the thrust configurations as inputs.

The influence of environment parameters and the robot's structure is investigated. A robot model capable of moving in a two-dimensional environment is developed correspondingly, which supports further studies' field tests of micro-robots targeting transport.

I. Introduction

Cancer has become one of the main diseases affecting human health. One common treatment for cancer is chemotherapy. However, a disadvantage of chemotherapy is that it indiscriminately attacks normal cells. According to Asma Saleem Qazi and K. Tariq [1], chemotherapy often decreases white blood cells, which may increase the risk of infection. In contrast, targeting transport provides a more precise curative effect on the diseased area, reducing damage to normal cells. Therefore, targeting transport is becoming an emphasis in the medical field.

However, traditional targeted therapy relies on recognizing chemical signals from substances, which inherit problems from chemotherapy. According to Gerber [2], the most significant impact of conventional targeted therapy is the amount of optimal dosing for best effectiveness, which motivates the development of other methods for targeted therapy.

Recent researchers studied the wide use of E. coli in the medical field. The studies motivated us to build a swimming robot for target transportation. According to Wang [3], a miniature robotic swimmer can access unreachable regions in the human body non-invasively. This motivates us to build a robot with controllable motion to perform more precise target transportation.

The high-viscosity liquid environment of human body limits the motion of typical macroscopic robot swimmers. According to Purcell [4], any symmetrical motion is invalid in such a liquid environment, so one method is to focus on asymmetric motion. In this case, microorganisms living in this environment that can move freely are considered. This research chooses E. coli as the fundamental model because of its simple structure. E.coli bacteria only have a single or two flagella and a regular body shape. The motion is easy to simulate and the shape is easy to be edited. Since the mass and volume of the flagella are small enough to be neglected, pure input forces are used during the project, instead of analysing the rotation of flagella. Therefore, an E.coli-based structure and corresponding control model is valid to be implemented for the micro-robot swimmer design.

This research focuses on designing the mechanical features of the swimming robot, validating the design with simulations, and developing the control model for path planning, trajectory tracking, and automatic error correction. Also, a plan for performing future tests to validate the design, and the discussion of challenges to building a micro-scale robot are put forward. This design aims to offer a feasible solution for future research in controlling Robot-Swimmer motions to enhance dosing precision and prevent side effects.

II. Methods

A. CAD

The robot's CAD model features a spherical body with four attached flagella to provide thrust. These flagella are capable of rotating to generate thrust, and each features a double helix structure. To balance the torque, two flagella were modeled clockwise and the other two counterclockwise. The CAD model is shown in Fig. 1 and Fig. 2. The body is a sphere with a diameter of 10 mm, and the flagella are 10 mm long.

B. CFD Analysis

CFD simulations were conducted on the flagella to optimize the design. According to the research conducted by Danis et al. [5], for a double helix structured flagella, the angle between the two helices influences the thrust force. The angle is shown in Fig. 3.

Various values of the angle between the two helices were modeled and tested in CFD analysis to find the maximum force they can provide. The multiple reference frame (MRF)

* These authors contributed equally to this work.
1 Department of Mechanical Engineering, University of Michigan, Ann Arbor, MI 48109, USA

979-8-3503-8803-9/24/$31.00 ©2024 IEEE

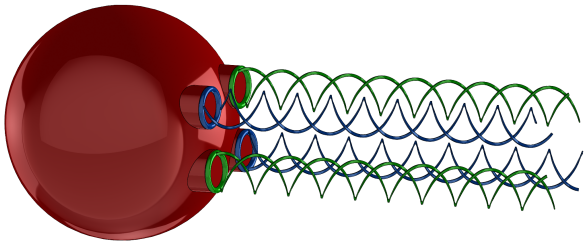

Fig. 1. CAD model of the whole robot

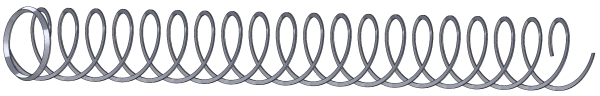

Fig. 2. CAD model of the flagellum

method was used in the simulation, with inlet and outlet pressures set to 12 kPa (gage), fluid density at 1060 kg/m^3, and viscosity at 4 cp to mimic the properties of blood. The rotational speed of the flagella was 1000 RPM, with the realizable k-ϵ turbulence model used.

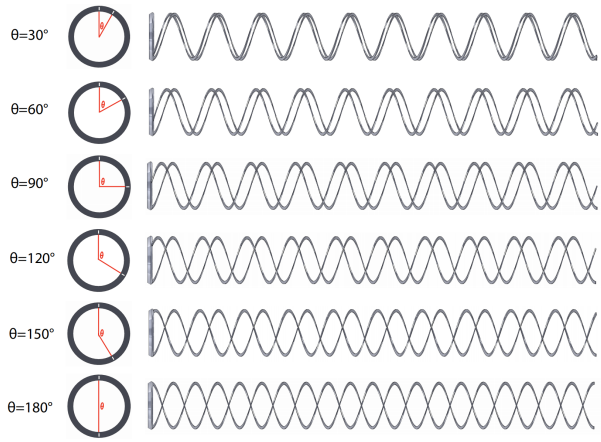

Fig. 3. All flagellum configurations tested in CFD simulation. θ is the angle between the two helices

C. Kinematics

The free-body diagram is shown in Fig. 4. According to the analysis by N. Lukerchenko et al. [6], a sphere moving in a liquid environment experiences three forces and one torque from the environment. Thrusts generated by a symmetrical set of flagella are combined into a single thrust in a 2-D plane, denoted as F_1 and F_2. The distance between F_1 and F_2 is d. In Fig. 4., the body rotates counterclockwise so F_2 is larger than F_1 to make the body rotate. Additionally, assume the velocity vector has an angle θ to the horizontal axis.

Considering the small size and viscous liquid environment, the Reynolds number is much smaller than 1 ($Re \ll 1$), so the form of Stokes Drag applies. According to Bird et al. [7], for a small sphere moving through a viscous fluid, the drag force can be described by the expression below:

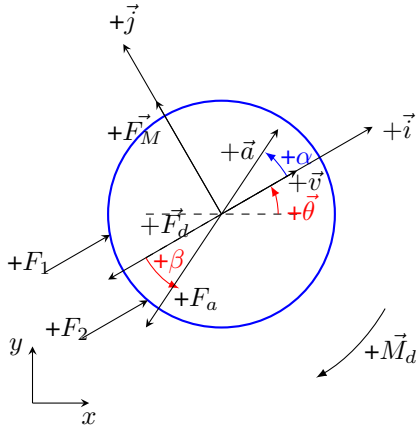

Fig. 4. Dynamic Model of the ideal sphere moving in fluids. F_1 and F_2 are thrust forces. F_d is the drag force. M_d is the drag torque. F_M is the Magnus force. F_m is the added mass force. θ is t is the angle between the velocity and fixed X axis. α is the angle between the acceleration and velocity.

$$\vec{F_d} = -6\pi\mu r\vec{v} \tag{1}$$

μ is the dynamic viscosity of the liquid. r is the radius of the sphere, and $\vec{v}$ is the velocity of the robot. For vector representation, the direction of the drag force is always opposite to the direction of velocity.

For the drag torque, the rotational Reynolds number of the body is $Re_\omega = \frac{\omega r^2}{\nu}$, where ω is the angular velocity, r is the radius of the sphere, and ν is the kinematics viscosity of the fluid. After calculation, the rotational Reynolds number Re_ω of the robot is much smaller than 1 ($Re_\omega \ll 1$). Hence, the drag torque can be expressed as the formula below defined by N. Lukerchenko [8]:

$$\vec{M_d} = -8\pi\mu r^3\vec{\omega} \tag{2}$$

$\mu = \nu\rho$ is the dynamic viscosity of the fluid with density ρ. For vector representation, the direction of drag torque is always in the opposite direction of the body's rotation.

The Magnus force, according to Rubinov and Keller [9] and Nigmatulin [10], has a general formula:

$$\vec{F_M} = C_M\rho\,(\vec{\omega} \times \vec{v}) \tag{3}$$

Tsuji et al. proved when ($Re \ll 1$) and ($Re_\omega \ll 1$), the coefficient of Magnus force C_M is approximately $\frac{3}{4}$ [11]. Both Re and Re_ω of the robot satisfies the requirement, so C_M equals $\frac{3}{4}$ in equation (3). Finally, when the sphere moves in liquid, added mass force is acted on the sphere. From Shuang Ghassemi et al. [12], the coefficient of added mass force C_m for an ideal sphere is $\frac{1}{2}$, so the added mass force has the formula below:

$$\vec{F_m} = -\frac{1}{2}\rho\vec{a} \tag{4}$$

$\vec{a} = \frac{d\vec{v}}{dt}$ is the acceleration of the body. The direction of the added mass force is in the opposite direction of acceleration.

To describe it clearly, the body-fixed coordinate system is constructed. The i direction points toward the body's velocity, while the j direction is oriented $90°$ counterclockwise to the i direction. Let β equals the angle between acceleration and velocity. The value of β can be expressed as:

$$\beta = \tan^{-1}\left(\frac{a_j}{a_i}\right) \tag{5}$$

a_j equals to the acceleration in the j direction, $a_j = a\sin\beta$, and a_i equals to the acceleration in the i direction, $a_i = a\cos\beta$. After using Newton's Second Law to describe linear motion and Euler's Law to describe rotation, the comprehensive kinematic equations can be summarized as:

$$ma_i = F_1 + F_2 - F_D + F_m\cos\beta \tag{6}$$

$$ma_j = F_M - F_m\sin\beta \tag{7}$$

After substituting the variables' expressions into the formulas above, the expressions are as follows:

$$ma_i = F_1 + F_2 - 6\pi\mu r v - \frac{1}{2}\rho a\cos\beta \tag{8}$$

$$ma_j = \frac{3}{4}\rho|\vec{\omega}\times\vec{v}| - \frac{1}{2}\rho a\sin\beta \tag{9}$$

Also, apply Euler's Law to the rotational process:

$$I\alpha = (F_1 - F_2)\frac{d}{2} + M_d \tag{10}$$

$\alpha = \frac{d\omega}{dt}$ is the angular acceleration. After substituting the variables' expression into the formulas above, the expression for rotation is as follows:

$$I\alpha = (F_1 - F_2)\frac{d}{2} - 8\pi\mu r^3\omega \tag{11}$$

The parameters used in this paper are listed in TABLE I:

Symbol	Representative	Magnitude
C_M	Magnus force coefficient	0.75
C_m	Added mass force coefficient	0.5
μ	Dynamic viscosity	$0.004\,\mathrm{N{\cdot}s/m^2}$
ν	Kinematics viscosity	$3.77\times10^{-6}\,\mathrm{m^2/s}$
m	Mass of the body	$5.55\times10^{-4}\,\mathrm{kg}$
D	Diameter of the body	$6.25\times10^{-3}\,\mathrm{m}$
r	Radius of the body	$3.125\times10^{-3}\,\mathrm{m}$
d	Distance between flagella on each side	$4.167\times10^{-3}\,\mathrm{m}$
ρ	Density of liquid	$1060\,\mathrm{kg/m^{-3}}$
I	Second moment of inertia of the body	$5.55\times10^{-9}\,\mathrm{kg{\cdot}m^2}$

TABLE I
LIST OF PARAMETERS

The variables used in this paper are listed in TABLE II:

Symbol	Representative
v	Velocity of the body
a	Acceleration of the body
a_i	Acceleration in i direction
a_j	Acceleration in j direction
ω	Angular velocity
α	Angular acceleration
Re	Reynolds number
Re_ω	Rotational Reynolds number
F_1	Upper thrust
F_2	Lower thrust
F_d	Drag force
M_d	Drag torque
F_M	Magnus force
F_m	Added mass force
θ	Angle between velocity and x axis
β	Angle between acceleration and velocity

TABLE II
LIST OF VARIABLES

D. Control

1) Route Planning Methods: To fulfill the requirement of obstacle avoidance and object tracking, a path-planning method is implemented for the swimming robot's navigation. According to Gasparetto et al. [13], systems with constraints on kinematics and dynamic environments possess path-planning problems. The path planning procedures can be configured as two basic steps: obstacle avoidance and object tracking.

For obstacle avoidance, road-map techniques are used to solve problems. The general obstacle avoidance method generates nodes among available areas for motion so that the fragments of feasible paths will be formed for the complete route.

For reference tracking, the overall goal is to calculate and select an optimized route with a minimum path cost. An example of the evaluation function for minimum cost is A^* algorithm, according to Candra et al. [14], which takes the form below:

$$f(n) = g(n) + h(n) \tag{12}$$

$f(n)$ represents the evaluated total cost, $g(n)$ represents the cost incurred from the initial state to n state, and $h(n)$ represents the estimated cost to arrive at a destination from n states. The three components cover the state of past, present, and future costs, which makes the algorithm heuristic-based, according to Hart et al. [15].

2) Feedback Control: The main task for navigation is to develop a control model to track the target. The system allows self-correcting the deviation between the desired route and the actual route. The structure of this system is shown in Fig. 5, based on the basic structure of feedback control systems, according to Franklin et al. [16]:

It consists of the controllers ($D_{c1}(s)$ and $D_{c2}(s)$), which is a set of models that scales the error signal. The plant($G(s)$) models the combination of the actuators and the process. While the actuators represent the generation of the input signal (force, torque, etc.), the process represents the overall

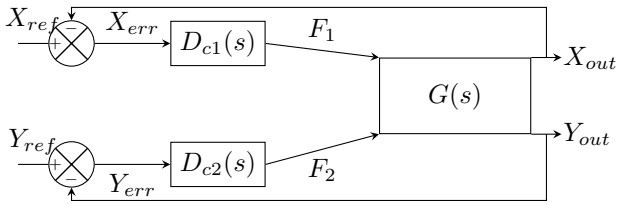

Fig. 5. Feedback Control Loop Designed

dynamics of the whole system. In this model, the plant modeling corresponds to the kinematics of the robot swimmer, representing the body's motion under the thrust forces (F_1 and F_2) and all the reaction forces.

The block diagram Fig. 5 represents the structure of the feedback loop. It takes in 2 parallel input signals X_{ref}, Y_{ref} as reference route, and generates X_{out}, Y_{out} as the actual route by the whole model, with X_{err}, Y_{err} as the error function between the reference and the output:

$$X_{err} = X_{ref} - X_{out} \tag{13}$$

$$Y_{err} = Y_{ref} - Y_{out} \tag{14}$$

The essence of the feedback loop is the comparison of the reference signal to the output signal. By minimizing the difference between the reference signal and the output signal, the whole system is being stabilized. The closed-feedback loop has a better stabilization effect than the open-loop control system, according to Bechhoefer [17].

PID controller ($D_c(s)$) is implemented for the system, which took the form below, according to Franklin et al. [16]:

$$D_c(s) = k_P + \frac{k_I}{s} + k_D s \tag{15}$$

k_P represents a simple scaling of the current incoming signal, k_I represents the integration of the past changes, and k_D represents the estimation of the future trend, which is provided by the info from the derivative.

In this way PID controller can take the change of the input/output signal from past, present, and future trends.

3) Feedforward Control: This program allows our robot pass through a set of target points to reach the final position. Our system generates n target points based on information detected by the sensors. These points are only distributed in a very small range, which is used to let our robot approximate the final target.

Fig. 6. is the block diagram that represents the concept of our feedforward control. Providing the given reference points, which are the x and y coordinates, the values are introduced into the controlling program. With the given value, the plant will manipulate the flagella and provide the forces needed. Here, $G_X^{-1}(s)$ and $G_Y^{-1}(s)$ is constructed from the dynamic model, with given equations, the program can solve the forces needed. These forces are generated by the rotation of the flagella. With a different speed of the four flagella, the robot is able to show multiple kinds of motion like swimming in a straight line, turning around, and floating. After the whole process, the system outputs the actual x and y coordinates the robot reaches.

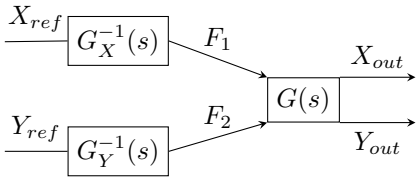

Fig. 6. Feedback Control Loop Designed

The controlling system is based on Newton's Second Law and Euler's equation of motion. The equations are established in a Cartesian coordinate in the x, y, and z directions. By solving the dynamic model equations, the program can provide the force each propulsor should generate. These forces allow our robot to form a uniformly accelerated motion in the x, and y directions separately, which in combination becomes a curvilinear motion. The motion allows the robot to go from one position to another in a short segment of time. The motion accumulates together so that it can reach the final position without error theoretically.

III. Test Results

A. CFD

Fig. 7 illustrates the magnitude of the thrust force generated by a single flagellum. The simulation results revealed that the maximum thrust was attained when the angle between the two helices was $180°$.

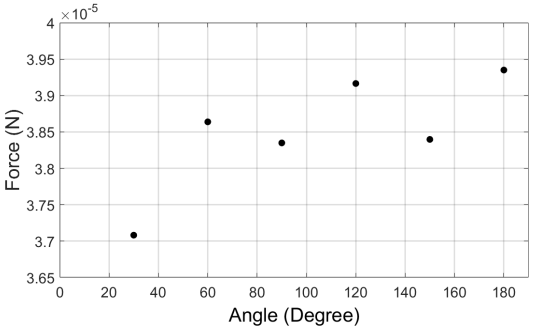

Fig. 7. Thrust force generated by a single flagellum at different θ. θ is the angle between two helices.

B. Control

1) Path Planning: The route from path planning on a given map is shown in Fig. 9 in red lines, based on the work of the code from Muhammet [18].

2) Feedback Control: The performance of the feedback loop's tracking behavior is evaluated by two parallel ramp inputs, as shown in Fig. 10, with planned route in the X and Y coordinate components separated. The labels are corresponding to those in the block diagram of Fig. 5.

The force configuration interpreted by the control loop is shown as Fig. 11, with labels corresponding to the block diagram of Fig. 5.

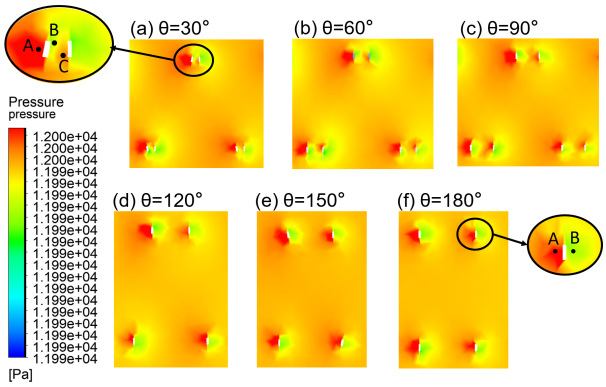

Fig. 8. Pressure contours plotted at the center-plane along the flagella at different θ. θ is the angle between two helices.

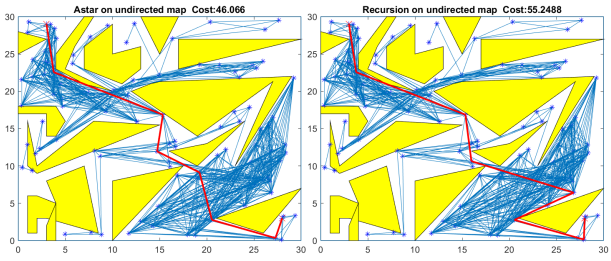

Fig. 9. Path Planning Comparison of A^* and Recursion Method

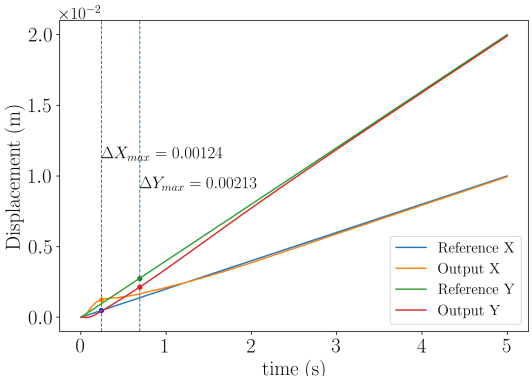

Fig. 10. Performance Evaluation of the Ramp Reference (X_{ref}, Y_{ref}) and Output Signal (X_{out}, Y_{out})

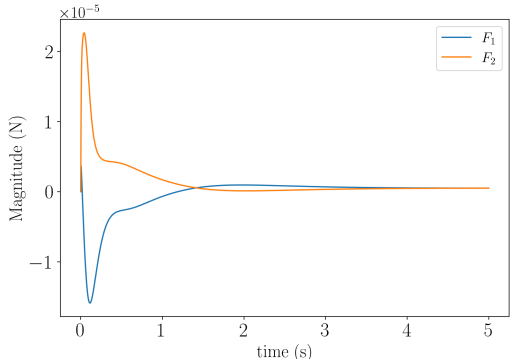

Fig. 11. Force Configuration (F_1, F_2) generated by the feedback system

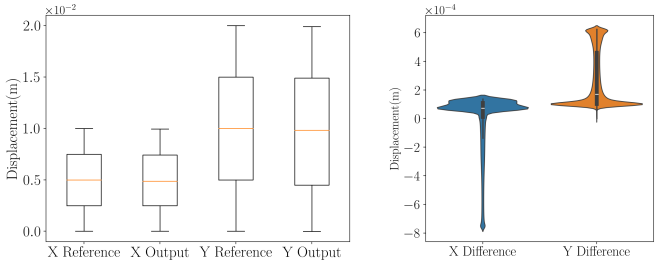

Fig. 12. Distribution of Reference, Output, and Error Signals (X_{ref}, Y_{ref}, X_{out}, Y_{out}, X_{err}, and Y_{err})

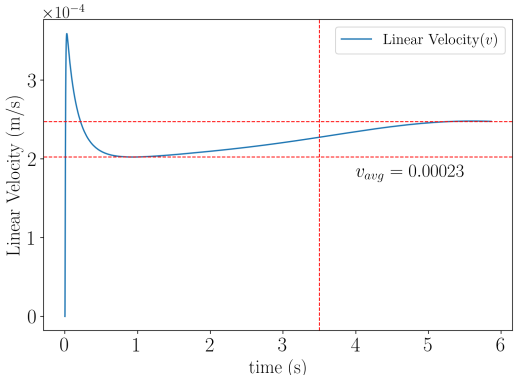

Fig. 13. Linear Velocity Distribution

The evaluation graph of the reference, output, and error signal are shown in Fig. 12, with labels corresponding to those in block diagram of Fig. 5.

The linear velocity distribution and the angular velocity distribution are also shown as Fig. 13 and 14.

3) Feedforward Control: Fig. 15. are the force configuration interpreted by feedforward control changing with respect to time. F_1 is the force generated by the propulsor on one side and F_2 is the force on the other. Each level of segment represents the magnitude of force needed between two targets. Fig. 15. on the top shows the phenomenon of forces during motion. The bottom figure is a zoom-in version of the top figure. Despite the impulse, the magnitude of the forces generated by the feedforward control system is approximately at the level of 10^{-3} N from Fig. 15. on the bottom.

Fig. 16. is the plot of the tracking behavior of our robot during its motion. Our team provides a straight-line route for convenient observation. This plot shows that our robot moves along its reference with small error. The actual output slightly leads to the reference for both x and y coordinates.

Fig. 17. are box plots that provide the comparison of the reference, actual output, and error signal of the x and y coordinate data. For the first 25% of the data, the output leads the reference for both the x and y coordinates, meaning that the actual output is slightly higher than the reference. For the last 25% of the data, the values are almost the same.

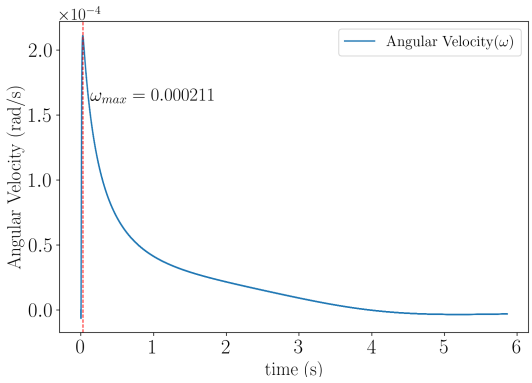

Fig. 14. Angular Velocity Distribution

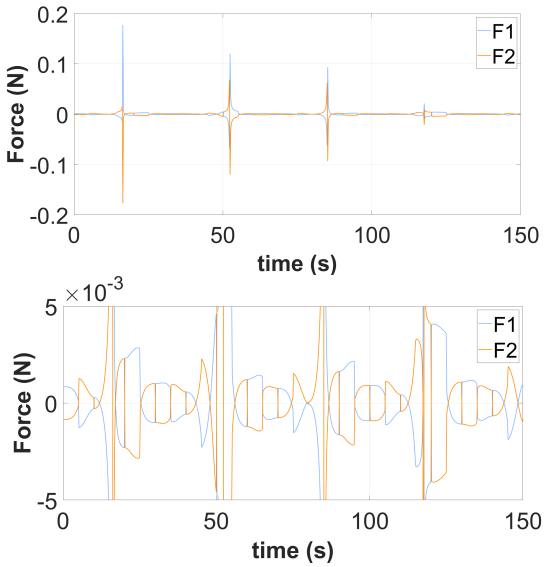

Fig. 15. Force configuration of feedforward control: the top figure shows the force configuration of the feedforward control, the bottom one is the zoom-in version

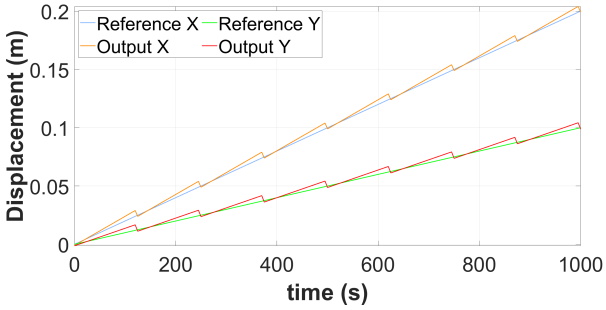

Fig. 16. Performance Evaluation of Feedforward Control

IV. Discussions

The development of a bio-inspired robotic system for targeted drug delivery is crucial to bridging existing technological gaps. To explore the necessary specifications for such a system, our team conducted a model-based investigation focusing on hydrodynamics, path planning, and robot control. This model will be assessed against specific requirements for

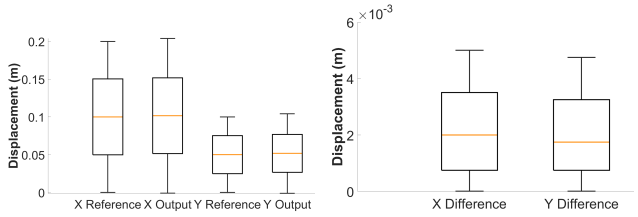

Fig. 17. Distribution of Reference, Output, and Error Signals

a decimeter-scale robotic system to determine the feasibility of creating an upscaled version. Our initial findings provide valuable insights into this complex challenge and represent a significant step toward the realization of a robotic system tailored for targeted drug delivery.

A. Discussion of results

1) Modeling: Numerical and Physics Based: To verify the model, the condition of the formulas should be met first. According to Bird et al. [7], N. Lukerchenko [8], Tsuji et al. [11], and Shuang Ghassemi et al. [12], the precondition of using formula (1), (2), (3), (4) is $Re \ll 1$ and $Re_\omega \ll 1$.

To calculate Re and Re_ω, the parameters needed are the kinematic viscosity μ = 0.004 N·s/m^2, and the density of liquid ρ = 1060 kg/m^{-3}. These values match those of the human blood according to Brindise et al. [19] and Piemjaiswang, R et al. [20]. From the CAD model, the diameter of the body is 6.25 mm. Based on the feedback control, the mean steady-state moving velocity is 2.3×10^{-4}m/s and the maximum angular velocity is 2.11×10^{-4}rad/s, shown in Fig. 13 and 14. The Reynolds number is $Re = \frac{\rho v d}{\mu}$ and the angular Reynolds number is $Re_\omega = \frac{\omega r^2}{\nu}$. Substitute the value of μ, ρ, d, ν into the formula of Re and Re_ω. The results are Re = 0.38 and Re_ω = 5.46×10^{-4}. Both the Re and Re_ω are much smaller than 1. This meets the condition of using formula (1), (2), (3), and (4).

2) CFD: In this study, CFD simulation was utilized to determine an optimal propeller shape that can generate larger thrust. As shown in Fig. 7, the thrust force is maximum when θ = 180°. When θ decreases, the thrust force also decreases, although this trend is not strictly consistent. To explain this trend, pressure contours are plotted in Fig. 8. In the pressure contours, points A and C exhibit relatively high pressure, while point B exhibits relatively low pressure.

A comparison of the pressure contour at θ = 180° and θ = 30° indicates that the pressure difference between points A and B is smaller when θ = 30°. This is due to the proximity of the high-pressure zone A and the low-pressure zone C, allowing the high-pressure zone and low-pressure zone to influence each other more easily. Consequently, when θ = 30° the pressure difference between A and B is smaller.

In the case of the flagellum with helices positioned 180° apart, the high-pressure zone A and the low-pressure zone C are not close to each other, resulting in a greater thrust force. Consequently, the final design adopted a double-helix

structure with the flagella positioned 180° apart to maximize the thrust force.

Based on the CFD analysis, the thrust force configuration is in 10^{-6} to 10^{-4} scale, addressed by feedback/feedforward, from system dynamics.

3) Path Planning: The initial goal of the path planning model is to offer a form of reference route for robots. Thus, the robot can perform obstacle avoidance and reference tracking to the specified target point from the reference route provided.

Based on Fig. 9, while the conventional recursion method gets a total route cost of 55.249, A^* got a total route cost of 46.066. Compared with the recursion method, the A^* route planning performs better while maintaining the obstacle avoidance performance.

External tools and sensors are applied to sense and map the environments and the obstacles. The available route is generated inside the robot based on the relative coordinates of the obstacles and reference points. Thus, the path planning algorithm is applied inside the robot to generate the mapping and the available trajectories before the whole motion.

The current path planning simulation focuses on static obstacles and does not account for dynamic obstacles. Future work should prioritize dynamic mapping of the environment, including the proper detection of moving obstacles for the robot to avoid.

4) Feedback Control: The force generated by the feedback control system, as shown in Fig. 11, is maintained within the magnitude of 10^{-6} N. Such magnitude is reasonable based on CFD analysis. From Fig. 10 and Fig. 17, the output slightly lags the reference in the X component, since it has the X_{err} distribution more on the negative region ($X_{err} < 0$), while the output mainly leads the reference in the Y component, since it has the Y_{err} distribution more on the positive region ($Y_{err} > 0$). The first 25% and the last 25% distributions between X_{ref} and X_{out}, and between Y_{ref} and Y_{out}, are generally on the same levels. Such a result indicates that the output signals maintain acceptable tracking behavior towards the reference and do not create significant overshoot behavior.

To achieve the expected controlling behavior, a low-level controller onboard is required. The onboard controller closes the control loop, compares the difference between the reference route and the actual route, and self-corrects the thrust configuration for tracking purposes with low latency. Such performance is less likely to be achieved by high-level controllers due to latency from wireless communications.

5) Feedforward Control: In Fig. 15., the magnitude of the force generated by the feedforward control system is maintained within the magnitude of 10^{-3} N. The value is higher than the force provided by the feedback control loop. This is because the control doesn't have a returning signal to fix the error generated during motion. Although this method has higher efficiency, the accuracy would be lower than feedback control. The forces F_1 and F_2 have the same magnitude in the opposite direction. The minus sign here represents the rotation direction of the flagella in the opposite direction. Thus, the flagellum provides a thrust force and balances the torque during motion. There are impulses observed in the figure coming from errors between reference and actual output. Forces are provided to fix the error to improve accuracy. Even though the impulse force is high, it only acts in an instant. Thus, the impulse motion won't cause much error deviating from its original direction.

In Fig. 16, the behavior plot shows that the actual motion is slightly higher than expected, causing the error. However, under ideal conditions, this feedforward controlling program can correct the error before the next segment of route starts. This correction process is only tested under a non-disturbance environment.

Observing from Fig. 17. the mean value of the error is about 2% of the actual motion, which is acceptable for our motion control. Also, the error for the y coordinate is smaller than the error for x. This is because the reference of the displacement for y is smaller than x. The phenomenon represents that as the distance goes further, the error would increase. The displacement of y is about half of the displacement of x.

To achieve the best controlling performance, a combination of Feedforward and Feedback control should be made. However, If the predictive model used for feedforward control is inaccurate, or if there are measurement delays, the combined system may not perform optimally. Additionally, implementing both types of control can be more complex and costly than using one type alone, so the benefits must be balanced against these factors.

B. Guidelines for Tests

A general guideline is provided for creating a physical embodiment of the robot and evaluating its performance.

1) Environment Setup: In order to replicate the flow of blood, it is essential to choose a fluid with comparable viscosity and density. A blood-mimicking fluid (BMF) can be utilized for this purpose. The BMF typically consists of glycerin, water, and anticoagulants, with the addition of red dyes to visually resemble blood.

A pool will be constructed to assess the robot's obstacle-avoidance capabilities. Various obstacles will be positioned within the pool to replicate the challenges the robot might face within the human body's blood vessels. The robot will then be immersed in the pool and directed by the system to navigate around the obstacles and proceed to its target.

2) Materials Choice: (i) Body: The robot's body can be built using 3D printing. Common materials can be Acrylonitrile Butadiene Styrene (ABS) or Polylactic Acid (PLA). *(ii)* Flagella: The flagella should be made of soft material to reduce damage to the human body. Soft material also maintains high resistance to deformation and ensures that the thrust force does not vary significantly due to deformation. Elastomers with high tear strength are a good choice, like some rubbers and synthetic elastomers can be

soft, stretchable, and have high toughness.

3) Data Collection and Processing: The accelerometer and speedometer inside the robot will be detecting the acceleration and velocity of its real-time motion. The real-time motion is then compared with the reference trajectory to derive the error, which is to be eliminated by the robot's error correction by the controller effect.

The ultrasonic generator/receiver will detect the relative position of the moving obstacle from itself. The map inside the robot will be updated with the positions of the moving obstacles, based on the static map embedded, for the use of dynamic path planning to avoid the moving obstacles and reach the desired position.

The depth sensors/pressure sensors measure the depth of the robot's current position for potential depth adjustment.

Torque sensors in the motor can read the torque output of the motor, while the hall sensor can read the angular acceleration and velocity of the flagella linked to the motor. The torque, angular velocity, angular acceleration, and linear acceleration from the accelerometer can be used to derive the thrust force configuration acting on the robot.

C. Limitations and Key Challenges

1) Limitations and future improvements: The current shape of the robot's body is a ball, which results in increased resistance. As part of the optimization process, it is advisable to consider designing an ellipsoid body to minimize resistance. However, this modification would necessitate the development of new dynamics and mechanics models.

During the motion, when the robot changes direction, the body starts to rotate causing unbalance. To address this issue, a device can be installed at the center of the body to counteract the torque generated by the flagella. This device is able to rotate and balance out the torque, preventing the body from rotating unintentionally.

2) Key challenges that need to be overcome in building the robot on a micrometer scale: (i) Power supply: Providing power to a micro-robot can be quite challenging. Most batteries are too large to fit into a micro-robot, and smaller batteries have limited capacity and can be quickly depleted. *(ii)* Fabrication and Assembly: Due to the small size, robots cannot be constructed using conventional manufacturing methods. The connection between the flagella and the robot must also be assembled with great precision. *(iii)* Recycling: The micro-robot cannot degrade. It also cannot be metabolized out of the body because it moves through the blood vessels.

V. CONCLUSIONS

This research designed the mechanical features of the swimming robot, validated the design with simulations, and developed the control model for path planning, trajectory tracking, and automatic error correction. Also, suggestions of experiment set-ups of validation and challenges to building a micro-scale robot are discussed for future research.

REFERENCES

[1] M. B. Hossain and A. H. Haldar Neer, *Chemotherapy*, pp. 49–58. Cham: Springer International Publishing, 2023.

[2] D. E. Gerber, "Targeted therapies: a new generation of cancer treatments," *American family physician*, vol. 77, no. 3, pp. 311–319, 2008.

[3] Y. Wang, H. Chen, J. Law, X. Du, and J. Yu, "Ultrafast miniature robotic swimmers with upstream motility," *Cyborg and Bionic Systems*, vol. 4, p. 0015, 2023.

[4] E. M. Purcell, "Life at low reynolds number," in *Physics and our world: reissue of the proceedings of a symposium in honor of Victor F Weisskopf*, pp. 47–67, World Scientific, 2014.

[5] U. Danis, R. Rasooli, C.-Y. Chen, O. Dur, M. Sitti, and K. Pekkan, "Thrust and hydrodynamic efficiency of the bundled flagella," *Micromachines*, vol. 10, no. 7, 2019.

[6] I. K. Z. C. N. Lukerchenko, Yu. Kvurt and P. Vlasak, "Drag force, drag torque, and magnus force coefficients of rotating spherical particle moving in fluid," *Particulate Science and Technology*, vol. 30, no. 1, pp. 55–67, 2012.

[7] R. B. Bird, "Transport phenomena ," *Applied Mechanics Reviews*, vol. 55, pp. R1–R4, 01 2002.

[8] N. Lukerchenko, Y. Kvurt, Z. Chara, and P. Vlasak, "Experimental evaluation of drag rotation coefficient of the spherical particle," *Proceedings of Engineering Mechanics*, pp. 169–170, 2004.

[9] S. I. Rubinow and J. B. Keller, "The transverse force on a spinning sphere moving in a viscous fluid," *Journal of Fluid Mechanics*, vol. 11, pp. 447–459, Jan. 1961.

[10] R. I. Nigmatulin, *Dynamics of multiphase media*, vol. 2. CRC Press, 1990.

[11] Y. Tsuji, Y. Morikawa, and O. Mizuno, "Experimental Measurement of the Magnus Force on a Rotating Sphere at Low Reynolds Numbers," *Journal of Fluids Engineering*, vol. 107, pp. 484–488, 12 1985.

[12] H. Ghassemi and E. Yari, "The added mass coefficient computation of sphere, ellipsoid and marine propellers using boundary element method," *Polish Maritime Research*, vol. 18, 01 2011.

[13] A. Gasparetto, P. Boscariol, A. Lanzutti, and R. Vidoni, *Path Planning and Trajectory Planning Algorithms: A General Overview*, pp. 3–27. Cham: Springer International Publishing, 2015.

[14] A. Candra, M. A. Budiman, and K. Hartanto, "Dijkstra's and a-star in finding the shortest path: a tutorial," in *2020 International Conference on Data Science, Artificial Intelligence, and Business Analytics (DATABIA)*, pp. 28–32, 2020.

[15] P. E. Hart, N. J. Nilsson, and B. Raphael, "A formal basis for the heuristic determination of minimum cost paths," *IEEE Transactions on Systems Science and Cybernetics*, vol. 4, no. 2, pp. 100–107, 1968.

[16] G. F. Franklin, D. J. Powell, and A. Emami-Naeini, *Feedback Control of Dynamic Systems*. USA: Prentice Hall PTR, 4th ed., 2001.

[17] J. Bechhoefer, "Feedback for physicists: A tutorial essay on control," *Rev. Mod. Phys.*, vol. 77, pp. 783–836, Aug 2005.

[18] Muhammet and Y. Yang, "Robin0265/pathplanning_code: Forked code ver1," May 2024.

[19] R. Piemjaiswang, Y. Ding, Y. Feng, and B. Chalermsinsuwan, "Effect of temperature-dependent blood viscosity on low-density lipoprotein transport: numerical study," in *Journal of Physics: Conference Series*, vol. 1789, p. 012005, IOP Publishing, 2021.

[20] M. C. Brindise, M. M. Busse, and P. P. Vlachos, "Density-and viscosity-matched newtonian and non-newtonian blood-analog solutions with pdms refractive index," *Experiments in fluids*, vol. 59, pp. 1–8, 2018.